Liquid Nitrogen Cooling for Irradiation of Silicon Pixel Detectors for the CMS Experiment

by

Colin England

A thesis submitted to the

Faculty of the Physics Department of the

University of Colorado at Boulder in partial fulfillment

of the requirements for the degree of

Bachelor of Science in Physics with Honors

Department of Physics

Defended Nov. 1, 2023

Committee Members:

Professor Stephen Wagner, Advisor, Department of Physics

Professor John Cumalat, Honors Council Representative, Department of Physics

Professor JulieMarie Shepard-Macklin, Outside Reader, President's Leadership Class

England, Colin (Department of Physics)

Liquid Nitrogen Cooling for Irradiation of Silicon Pixel Detectors for the CMS Experiment

Thesis directed by Professor Professor Stephen Wagner

The upgrades to the High Luminosity Large Hadron Collider (HL-LHC) impose unique challenges on inner tracker pixel sensors for the Compact Muon Solenoid (CMS) experiment, necessitating changes outlined as the Phase-2 upgrade. A metric that will be crucial to the success of these sensors is their radiation hardness over a 10 year lifetime. In January 2023, the CMS RD53B readout chips (C-ROCs) were irradiated up to 100 MRad at Sandia National Laboratories over three days. In order to best simulate the real working conditions at the CMS experiment, keeping the chips at a cool, steady temperature is key. A liquid nitrogen cooling system was implemented to keep the temperature of the sensors and ROCs stable at -20 °C. This system maintained temperature sufficiently for much of the irradiation, but some larger than expected fluctuations occurred due to electromagnetic interference (EMI) and liquid nitrogen transfer. Several of the wire bonds connecting RD53B chips to readout electronics were destroyed during the irradiation, leading to an inconclusive result with multiple speculated causes. Follow-up tests at CU Boulder were performed to examine several causes of failure and improvements to the liquid nitrogen cooling system were made in anticipation of a return to Sandia National Laboratories.

Acknowledgements

I would like to thank my committee and especially Professor Wagner for guiding me through my work on this project. I am incredibly grateful to Professor Cumalat for helping me get involved with physics research. I would like to thank Zachary Franklin and Maxwell Herrmann for assisting with my work in the lab. Lastly, I would like to thank my parents for allowing me to become the person I am today.

Contents

Tables

Table

Figures

Figure

Chapter 1

Introduction

At CERN, the High Luminosity Large Hadron Collider (HL-LHC) is expected to begin operating in 2029. Located on the Large Hadron Collider is a large particle detector known as the Compact Muon Solenoid (CMS). The CMS experiment is considered general-purpose with several main goals in the area of High-Energy Physics (HEP). With proton-proton collision center-of-mass energies of 14 TeV and exceptionally high luminosity predicted, the CMS experiment will undergo important upgrades known as Phase-2 before operation of the HL-LHC begins. To survive the extreme conditions introduced by the HL-LHC, the Inner Tracker will have to withstand a dose of up to 1 Grad of radiation over 10 years. Thus, a large focus of developing the silicon sensors and electronics that will line the Inner Tracker is on their radiation hardness, a measure of resistance to damage from ionizing radiation [1, 2].

In order to collect tracker data in CMS, silicon sensors are bump-bonded to readout chips (ROCs). The RD53 Collaboration is developing ROCs to survive in the CMS Inner Tracker alongside the sensors. Three versions of RD53 ROCs have been in development, with the final iteration, RD53C, being intended for integration into the CMS and ATLAS experiments starting in 2026.

Several groups have performed various radiation hardness tests on RD53A chips. X-ray irradiation tests up to 2.2 Grad have been successful on RD53A chips. At CMS, RD53B readout chips and silicon sensors are kept at a constant temperature of -15 °C. While cool temperatures do not affect the mechanisms of radiation damage, they reduce the damage, which is seen as leakage currents, an effect of radiation on the silicon sensors [3, 4].

To best replicate these conditions, cooling the electronics in a high radiation environment is a necessary challenge for performing these tests. Due to the scale of the planned dose, performing tests at radiation facilities is the most realistic option. Many radiation facilities have constraints on what types of systems can be operated during irradiation. A major consideration is the effect of large amounts of radiation on any parts of the cooling system placed inside the array alongside the sample. Perhaps the simplest method of cooling, utilizing thermoelectric devices such as a Peltier cooler, would contain the entire cooling system inside the irradiation site with only cables needed to power the device running outside. The mechanism behind this style of cooling involves absorbing the heat inside the device and transporting it outside into a cooler environment. Due to the large amounts of heat in the cell at Sandia, efficiency concerns arise. Unfortunately, previous studies of semiconductors, a key design component of thermoelectric devices, suggest continuous damage at radiation doses starting below the scale of hundreds of Mrad. It is unlikely that this method of cooling would survive the intended radiation dose [7].

A possible alternative is an external cooling system that delivers coolant into the irradiation array. This minimizes the radiation exposure of the cooling system and could allow manual operation of the cooling system during irradiation. This thesis discusses the results of a January 2023 Irradiation of RD53B chips and presents an improved liquid nitrogen cooling system effective for smaller scale HEP experiments in high radiation environments.

Chapter 2

Background Information

2.1 The Standard Model and Beyond

The Standard Model of particle physics explains all currently known elementary particles and three of the four known fundamental forces in a unifying framework. It has predicted the discovery of several particles before experimental confirmation, with the most recent example being the Higgs boson in 2012. The theory divides all known elementary particles into two categories, matter particles called fermions and interaction carrier particles called bosons. The Higgs boson, only recently discovered but theoretically proposed decades ago, explains how particles have mass. Three of the four known fundamental forces can be explained by the exchange of bosons. These are the weak force, strong force, and electromagnetic force. While internally consistent in theory, the gaps in explanation of multiple phenomena within the Standard Model is a large motivating factor in the continued development of particle physics experimentation.

Several gaps in the Standard Model have been presented, typically as a result of discontinuities between theory and experiment. Perhaps the most known example is the gravitational force. Despite being the fundamental force most familiar to human life, it is not explained within the Standard Model. Attempts at the addition of a theoretical graviton particle alongside the other bosons that explain fundamental forces have not been reconciled with experimental observation of gravitational effects [8].

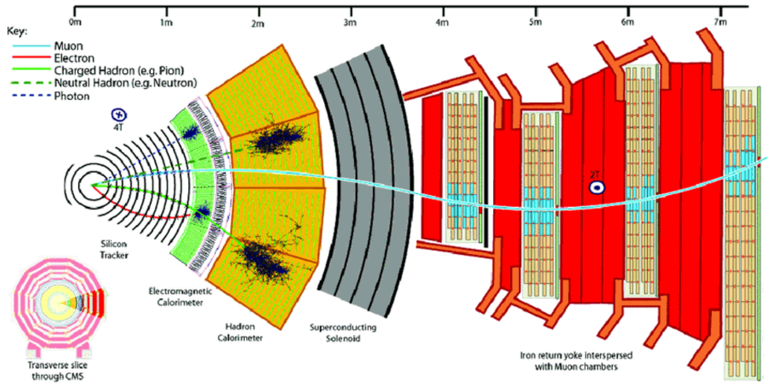

Figure 2.1: A slice of the layers of the CMS Experiment with examples of how charged particles could move through the different layers. Source: [10]

2.2 CMS Experiment Background

The Compact Muon Solenoid (CMS) is built on the LHC ring at CERN and its layout is constrained by a 4 Tesla solenoid magnet. This magnet bends trajectories of charged particles emerging from high-energy collisions in the LHC. Understanding the paths of these particles yields their charge and momentum, which are important properties of elementary particles in HEP. The CMS Experiment is multi-layered, with silicon pixel sensors and silicon strips surrounding the beam pipe. Since the pixels are the closest to the beamline they have the largest dose of radiation. In the next layer, the Electromagnetic Calorimeter made of lead tungstate determines the energy of electrons and photons by stopping them. Followed up by this is the Hadron Calorimeter, which similarly stops hadrons, particles governed by the strong interaction. The solenoid itself comprises the next layer, which at time of construction was the largest solenoid magnet ever built, generating a magnetic field 100,000 times stronger than that of the Earth. The final layer is comprised of muon detectors and a steel yoke to identify muons. The layered nature of the CMS Experiment is depicted in Figure 2.1 [9].

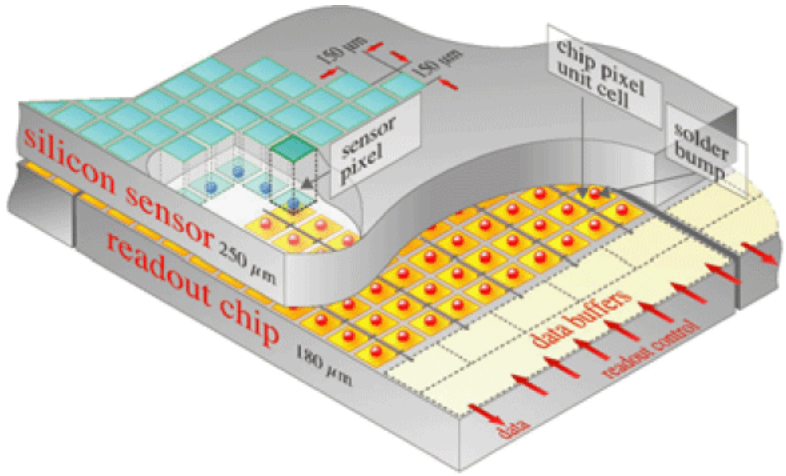

Figure 2.2: An illustration of a silicon pixel detector, consisting of both a silicon sensor and readout chip. Source: [12]

2.3 Silicon Sensors

A single silicon pixel sensor is made up of an array of tiny pixels of silicon. Each pixel will measure 25 µm by 100 µm in the CMS Phase-2 Upgrade. When a charged particle collides with a pixel, electrons are ionized from atomic structures, creating holes. An almost instantaneous electric signal is generated in the form of a small current. A voltage is applied by the readout chip to amplify the signal, giving crucial timing and charge information about the particle. With multiple layers of sensors, a three dimensional reconstruction of the particle's trajectory becomes possible [11].

N-in-p silicon pixel sensors have been designed to replace the previous n-in-n sensors. P-type silicon is created by adding impurities that create holes where electrons would normally exist. N-type silicon is created by adding impurities that cause it to be conductive. Combining both types of silicon with a creative biasing method has resulted in n-in-p silicon detectors. These n-in-p sensors are able to operate in the partially depleted state, thus increasing their radiation hardness [12]. A complete silicon pixel detector with silicon sensor and readout chip is depicted in Figure 2.2.

Chapter 3

Methods

3.1 Irradiation

In order to test the radiation hardness of RD53B readout chips and silicon sensors, they were irradiated at the Gamma Irradiation Facility at Sandia National Laboratories with a goal of 550 MRad in January 2023. Irradiation was performed via gamma irradiation from Cobalt-60 beta decay over a course of 2 weeks. At Sandia, ^{60}Co pins form a ring of approximately a foot wide around the sample with the radiation dosage maximized at the center of the circle. When a ^{60}Co isotope undergoes beta decay, it primarily has two paths: it emits an electron of energy 0.31 MeV or one of energy 1.48 MeV, becoming a Nickel isomer, ^{60}Ni as shown:

$$^{60}_{27}\mathrm{Co} \longrightarrow {}^{60^*}_{28}\mathrm{Ni} + {}^{0}_{-1}\mathrm{e} + {}^{0}\overline{\nu}_e \tag{3.1}$$

Due to nuclear instability, the ^{60}Ni quickly decays into a stable isotope of Nickel while emitting either one or two gamma ray photons as shown:

$$^{60^*}_{28}\mathrm{Ni} \longrightarrow {}^{60}_{28}\mathrm{Ni} + \gamma \tag{3.2}$$

For the 0.31 MeV beta path, the Nickel will decay first to a lower energy excited state, then to the ground state, emitting two gammas of energies 1.17 MeV and 1.33 MeV respectively. For the 1.48 MeV beta path, only a gamma of 1.33 MeV is released [13].

Due to the energy of the gammas, the main method of interaction with the electronics is Compton scattering, as depicted in Figure 3.1. In Compton scattering, an X-ray or gamma ray

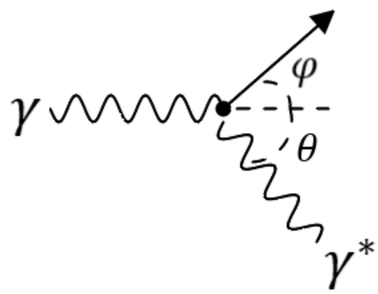

Figure 3.1: A Feynman diagram of Compton scattering.

photon (in this case the latter) collides with a charged particle (in this case electrons). This collision causes a shift in the photon's wavelength and transfers energy to the charged particle, which recoils. While statistically less probable, the gamma photons have sufficient energy to result in pair production. In pair production, a neutral boson transforms into a particle and antiparticle pair. In the case of a photon, this would mean converting its energy into an electron-positron pair. The necessary energy for this interaction can be determined by adding the rest mass energy of an electron and positron together, resulting in a required energy of 1.022 MeV from the photon. Moving from the theoretical possibility to the probability, the pair production cross section is notably proportional to the atomic number as shown:

$$\sigma = \alpha r_e^2 \, Z^2 \, P(E, Z), \tag{3.3}$$

where α is the fine-structure constant, r_e^2 is the classical radius of an electron, Z is the atomic number, and P(E,Z) is a complex-valued function of energy and atomic number. Examining the materials in the sample being irradiated, the silicon of the sensors and aluminum in the thermos are of note. Figure 3.2 shows the dominant regions of cross sections of compton scattering and pair production as a function of photon energy and atomic number. For silicon and aluminum, the atomic number and incident photon energies show that Compton scattering will dominate [14]

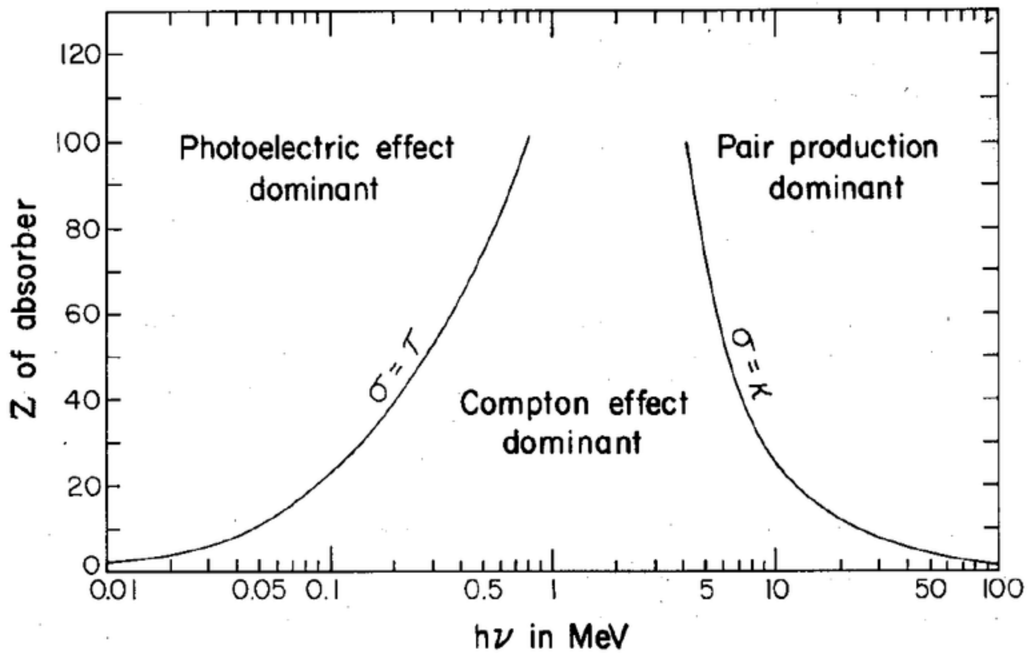

Figure 3.2: Regions where Compton scattering or pair production are dominant as a function of atomic number and photon energy. Source: [17]

Due to the nature of Compton scattering, it is expected for the nuclei to remain unperturbed with electronic bonding being the most likely part of the sample to receive damage. Compton scattering is an indirect form of ionizing radiation, as the photons are electrically neutral, but secondary ionization may occur in which an ejected electron ionizes other atoms [15].

3.2 Temperature Control

To replicate the temperature conditions at the CMS Experiment, a feedback-based liquid nitrogen cooling system was used to control the temperature during tests at Sandia National Laboratories. At CMS, the silicon sensors and readout chips are held at -15 °C via evaporative CO_2 cooling. This system was upgraded from a previous liquid phase cooling using C_6F_{14}. The primary constraints for designing these kinds of large scale cooling systems are compatibility with the arrangement and scale of the experiment as well as radiation hardness. In this scale, different constraints emerge due to the layout of the Gamma Irradiation Facility at Sandia National Labs.

The irradiation array used is approximately a foot in diameter which necessitates either an internal cooling system that can survive significant radiation, or an external cooling system that sends a coolant into the array. Additionally, the Gamma Irradiation Facility requires a cooling method that can be left unattended during weekends and overnight on weekdays. This results in a minimum 60 hour period from Friday evening to Monday morning in which no maintenance can be performed on a cooling system. To remain effective for 2 weeks, it is crucial that any method of cooling is resistant to radiation damage and corrosion damage.

With these constraints in mind for temperature control during tests at Sandia, a system has been designed that burns liquid nitrogen and delivers cold nitrogen vapor to the sensors and ROCs to maintain cool temperatures. This system mainly consists of a small dewar holding LN_2 and containing resistors that can boil the nitrogen inside, a transfer line to send the gaseous nitrogen to our thermos carrying the electronics, a transfer line/gravity feed apparatus for automatic refills controlled by a solenoid and level system, and finally a controlling circuit for the resistors. The circuit itself contains multiple power supplies with software control via a LabVIEW program that evaluates via feedback when to heat the resistors. A labeled image of the entire cooling system setup at University of Colorado Boulder can be seen in Figure 3.3.

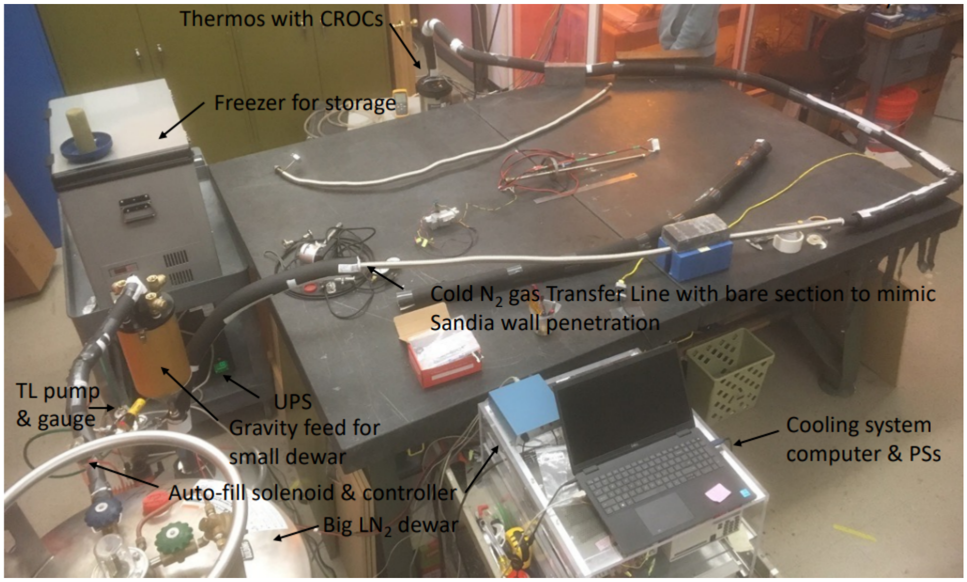

Figure 3.3: Labeled photo of the liquid nitrogen cooling system at CU Boulder.

To boil the liquid nitrogen, four 2.4 ohm resistors are connected in parallel inside the dewar and are provided between 0 and 14.9 amps. The heat provided to the liquid nitrogen can be calculated by using the formula for electrical power and integrating over time as shown:

$$Q = \int I^2 R \, dt, \tag{3.4}$$

where Q is the heat added, I is the current, and R is the total resistance of the parallel resistors. The parallel arrangement of resistors allows for greater power dissipation than an equivalent larger resistor due to increased surface area.

In order to adjust current across the resistors based on temperature, a power supply controlled by a computer was chosen. In order to control the resistors with this power supply, a control circuit is implemented as depicted in Figure 3.4. From left to right, a 10 kΩ potentiometer is set at 6.5 kΩ from ground to the inverting input of the non-inverting op-amp. Connected to the non-inverting input of the op-amp is the variable power supply controlled by the computer, which varies from +2 V to +4 V. The op-amp itself is an LF356N with +15 V and -15 V power supply voltages. This op-amp gives the signal from the programmable power supply a gain related to the configuration

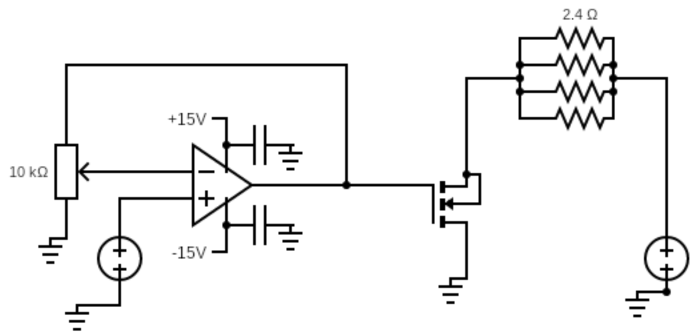

Figure 3.4: The control circuit used to reach currents between 0 and 14.9 amps.

of the potentiometer, as shown:

$$A = \frac{V_{out}}{V_{in}} = 1 + \frac{R_f}{R_{in}}, \tag{3.5}$$

using the 6.5 kΩ figure as R_{in} and the remaining 3.5 kΩ as R_f, we can calculate a gain A of about 1.54. From this calculation, the voltages output into the N channel MOSFET range from +3.08 V to +6.15 V. The 75321P MOSFET has a threshold voltage set such that no current flows at the lower end of the range of output voltages, with an exponential increase in current as these voltages increase. The source of the MOSFET is connected to ground whereas the drain is connected to the resistors. On the other side of the parallel 2.4 Ω resistors is an additional power supply held at a constant 10 V. This power supply can supply large currents in the target range. In order to accurately track the temperature inside the thermos, the cooling system utilizes type K thermocouples and a 20' long thermocouple extension cable to transfer the data outside the irradiation array. While several types of thermocouples work in the system's operating temperature range, type K thermocouples are noteworthy for their success in high radiation environments. Type K thermocouples work through the Seebeck effect in which a temperature difference between two points on a conductor generates a proportional electromotive force. A simple diagram of a standard type K thermocouple is shown in Figure 3.5. The long thermocouple extension cable is attached to a USB adaptor to be read by the LabVIEW program.

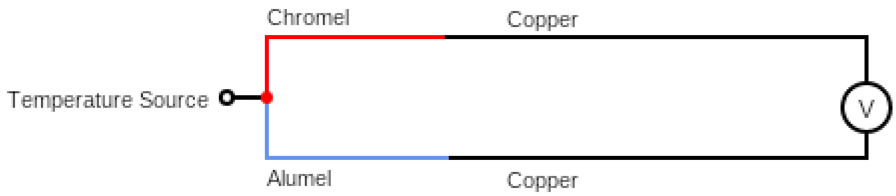

Figure 3.5: A diagram of a standard type k thermocouple.

3.3 Monitoring ROC Performance

Before and during irradiation, routine scans were performed to measure and calibrate the silicon pixels. Approximately every 30 minutes, the temperature, diagnostic voltages, and ring oscillator counts were measured through these scans.

Each RD53B readout chip is equipped with 42 ring oscillator circuits. A ring oscillator generates continuous waveforms when powered and is comprised of an odd number of inverters, sometimes called NOT gates, connected in series. The last inverter is connected to the first, outputting an oscillation between two voltages. An example of a simple ring oscillator circuit with three inverters can be seen in Figure 3.6. The frequency of this output has many applications, including studying the effects of temperature, voltage, and radiation hardness on a chip [16].

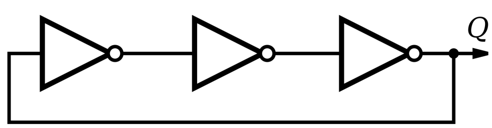

Figure 3.6: A diagram of a simple three inverter ring oscillator circuit. Source: [18]

Chapter 4

January 2023 Irradiation Results

In early January 2023, two RD53B chips wire bonded to readout electronics were irradiated via the methods outlined in the previous section. Unfortunately, the result was inconclusive with multiple possible sources of failure. Firstly, the temperature read-back inside the thermos was not always accurate, especially during liquid nitrogen transfers, and occasionally appeared to rise above the desired temperature of -20 °C. Secondly, the wire bonding between the readout chips and electronics failed as seen in Figure 4.1. Finally, a configuration mistake was made between two different ROCs. Due to the wire bond failure, no additional data was collected after 72 hours. A total integrated dose of 100 Mrad was reached before failure as seen in Figure 4.2. Some ring oscillator, diagnostic voltage data, and internal temperature data were recorded before the wire bond failure. Whether the wire bonds failed due to the temperature conditions, the radiation, the configuration error, or an unknown manufacturing error prior to irradiation is unknown. A future irradiation with proper temperature control should give more insight into what was responsible.

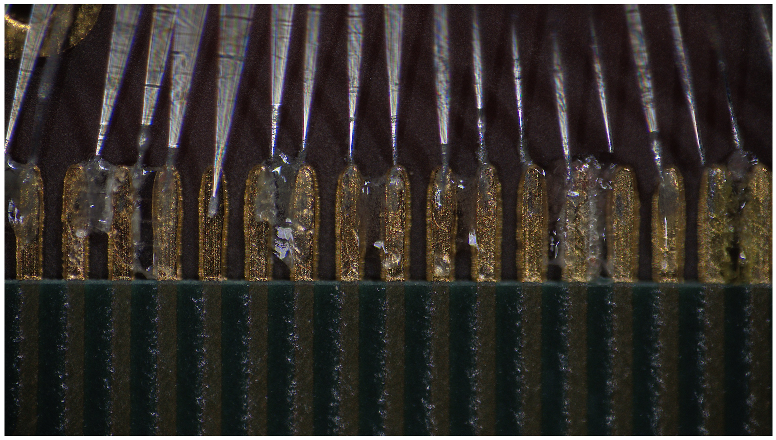

Figure 4.1: A photograph of the failed wire bonds taken under a microscope.

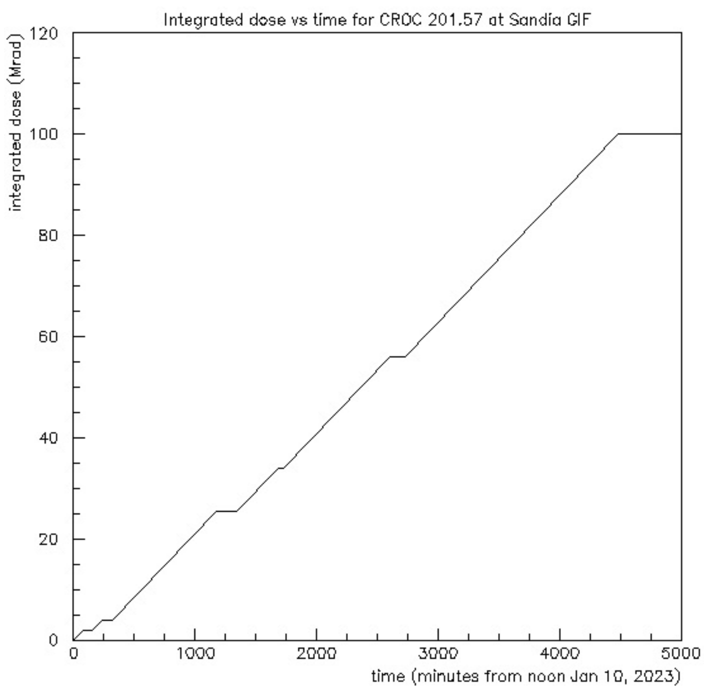

Figure 4.2: The actual total integrated dose (TID) over time during irradiation (earlier it is mentioned that it should be approximately linear on a two week timescale). Source: [19]

During irradiation, the ring oscillator frequency was monitored for sixteen different ring oscillator circuits to study the performance of the ROCs and pixels. With temperature and supply voltage constant, ring oscillator frequency is expected to be inversely proportional to radiation dose. During each ring oscillator scan, the number of oscillations was counted for a fixed time period. The ring oscillator count is directly proportional to the average frequency during a given scan. Plots of ring oscillator counts for two sets of eight ring oscillator circuits during irradiation can be seen in Figure 4.3. The behavior of ring oscillator counts and therefore frequency matched expectations, with a linear drop tracking the increase total dose.

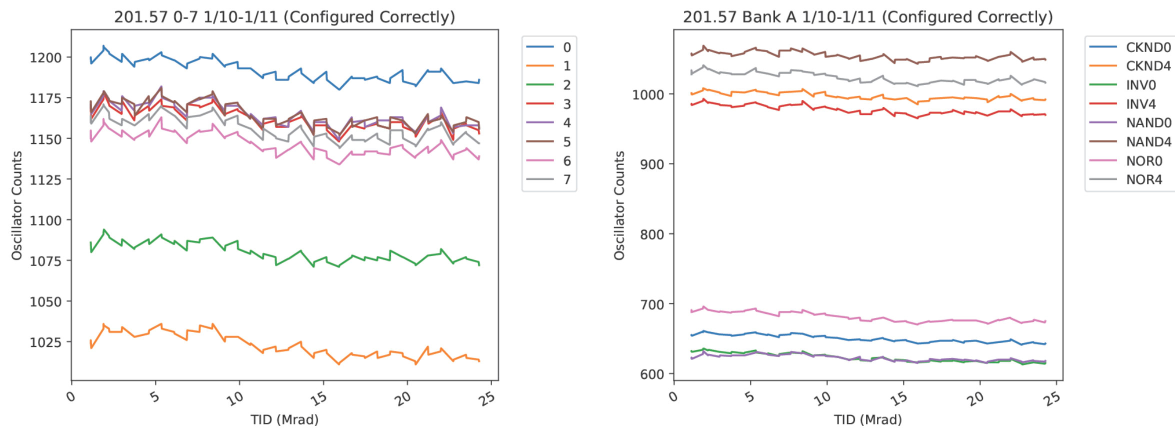

Figure 4.3: Plots of the oscillator counts of two groups of eight different ring oscillators during irradiation in January 2023. Irradiation dose was approximately linear, so a linear decrease in ring oscillator frequency is predicted and the result matches. Source: [19]

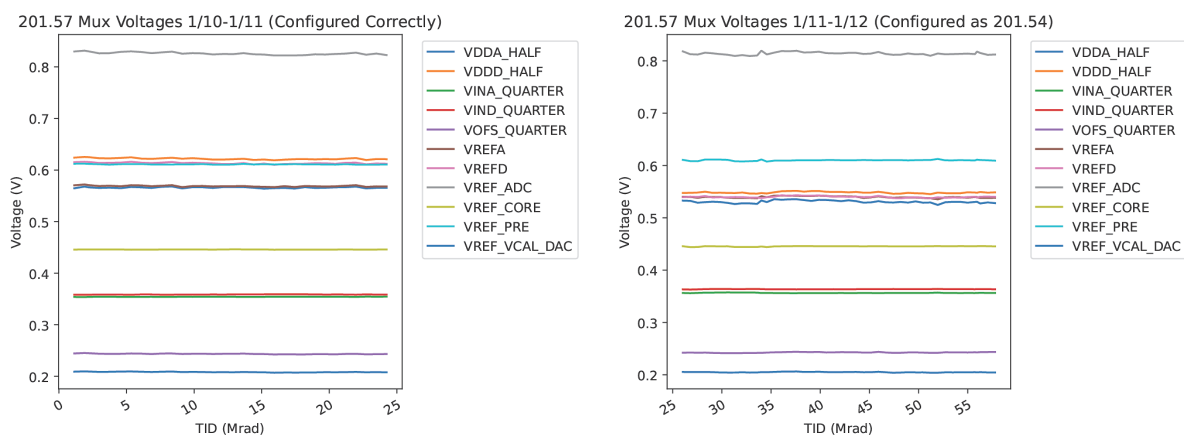

Figure 4.4: Plots of diagnostic voltages during stable configuration periods. All voltages are expected to remain constant unless an error is encountered. Source: [19]

As seen in Figure 4.4, several different diagnostic voltages were measured as the radiation dose increased. These voltages all remained stable during periods with no change to the configuration.

There are two speculated sources for the inconsistent temperature data, the first being noise in the temperature data and the second being the reaction of the temperature control to noise. In Figure 4.5, the temperature data recorded by the cooling system over the entire three days is plotted, measured via a long thermocouple line extending out of the array that reports temperatures 4 times a second. This plot can be compared with Figure 4.6, which has temperature measurements recorded during the first quarter of the irradiation via an internal temperature measurement by the ROC. With many outlying data points not present in the internal temperature measurements, it is speculated that the outliers in the thermocouple temperature data are noise caused by electromagnetic interference (EMI). The degree spike present in the internal temperature measurements is speculated to be caused by the response from the cooling system to temperature data noise. Possible causes and further reasoning for the presence of noise due to EMI will be discussed in the next section.

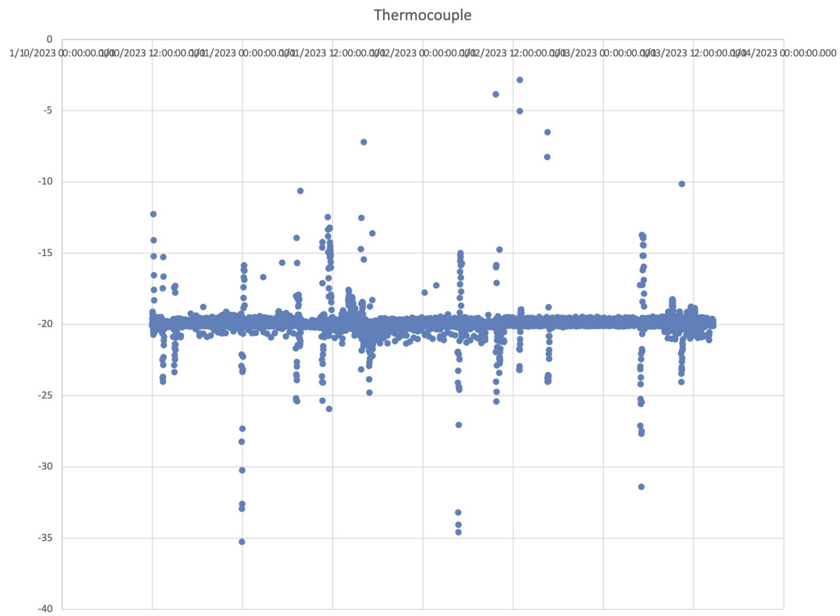

Figure 4.5: Plot of thermocouple temperature measurements taken over irradiation. Speculated sources of interference likely contributed to the outliers. Source: [19]

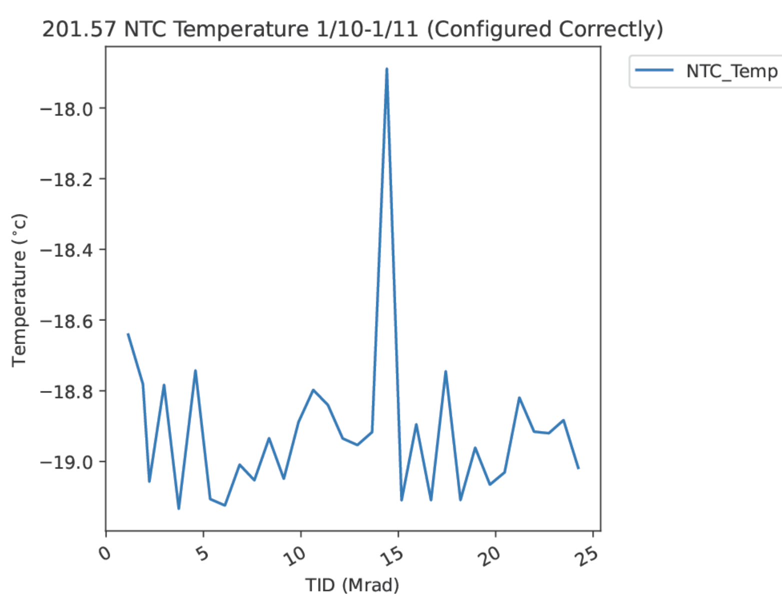

Figure 4.6: Plot of temperature (measured by ROC and less likely to have interference). The spike to -18 °C is likely due to poor temperature control. Source: [19]

In order to isolate potential causes of the wire bond failure, an irradiation with proper temperature control must follow-up this result. While some relationships were established with limited data, such as the ring oscillator behavior, the cause of wire bond failure is the most important question. Removing the inadequate temperature control as a potential factor is key to the success of studying future irradiation tests. In pursuing this, minimizing temperature data noise and reassessing how the cooling system responds to possible noise is crucial.

Chapter 5

Cooling System Improvements

5.1 Temperature Data Noise

Due to the order of magnitude of the voltage transferred along thermocouple lines being on the mV scale as seen in table 5.1, electromagnetic interference (EMI) has a high probability of interfering with temperature measurements and the temperature control that relies on them by inducing a voltage. Using a Baofeng UV-5R ham radio, signals of 139.800Hz were emitted in the vicinity of a type K thermocouple and 20” extension cable fully extended with no coiling. At a distance of 1 meter, turning on the signal of the ham radio changed the measured temperature of the room from 22.5 °C to 77.6 °C. It is feasible that the fastest change in current across the resistors of approximately 30 A/s could be responsible for the temperature data noise. In consideration for any source of EMI, metal braided shielding has been placed around the thermocouple and extension cable and grounded to the power supplies used to control the temperature control circuit.

Table 5.1: This table gives example conversions from temperature to electric potential difference for a type K thermocouple. Adapted from [20].

Temperature (°C)	Potential difference (mV)
-40	-1.527
-30	-1.156
-20	-0.778
-10	-0.392
0	0
10	0.397
20	0.798

5.2 Software Control Improvements

There are many considerations necessary for efficient software control of temperature, including time delay, data noise, the trade-off between efficiency and accuracy, and counteracting uncontrolled temperature changes. In LabVIEW, a variety of standard coding structures are available alongside standard mathematical computations. The simplest method of control would be a loop that checks the current temperature and the user set target temperature and compares them, deciding whether to set a voltage that burns liquid nitrogen or a voltage that doesn't. There are several issues that arise with this simple feedback loop.

While temperature data is transmitted to the laptop almost instantly, the effects of a change in voltage set by the LabVIEW program have a varying time delay. The change in current in the resistors is not instant due to the layout of the control circuit. Once liquid nitrogen is boiled, the nitrogen vapor must travel through 20 feet of transfer line to reach the thermos. If the transfer line is significantly warmer than the small dewar of liquid nitrogen, it will be cooled before the nitrogen vapor can begin cooling the thermos with electronics. Once an equilibrium state is reached, cool nitrogen vapor has filled the entire transfer line and additional burning of liquid nitrogen will exert pressure on the nitrogen vapor closest to the thermos, decreasing the time delay from when current in the resistors is changed to when a temperature change is detected. Since the vast majority of time operating the cooling system is in an equilibrium state near the set temperature, the most important time delay to consider is during this state. In order to account for time delay, a linear extrapolation algorithm was implemented that computes the average rate of change of temperature over the past 5 seconds and uses this rate to extrapolate the temperature 20 seconds into the future. The predicted temperature in 20 seconds is then used in comparison with the set temperature to decide how to adjust the current.

Due to the nature of type K thermocouple measurements, some temporary noise is anticipated in the temperature data. Noise in thermocouple measurements typically presents as outliers. Figure 5.1 shows a histogram of the magnitudes of changes in temperature during a liquid nitrogen cooling system test. The right, small peak in the distribution suggests the presence of noise. To minimize the impact of any possible noise, a point-by-point median of temperature data is taken to prevent non-physical spikes in temperature from interrupting the accuracy of temperature control.

One potential source of EMI noise is the large changes in current the cooling system is capable of generating. Instead of implementing two states, no current and maximum current, a stepping algorithm has been implemented with multiple benefits. The voltage of the controlled power supply is now adjusted by 0.1 V for each iteration of the program, resulting in a maximum of 0.4 V/s change. While the controlled voltage is directly proportional to the output current across the resistors, a polynomial or exponential relationship could not be established. The complexity of the circuit makes theoretical calculations difficult, so values of supply voltage and the resulting currents were recorded to ensure the change in current was limited.

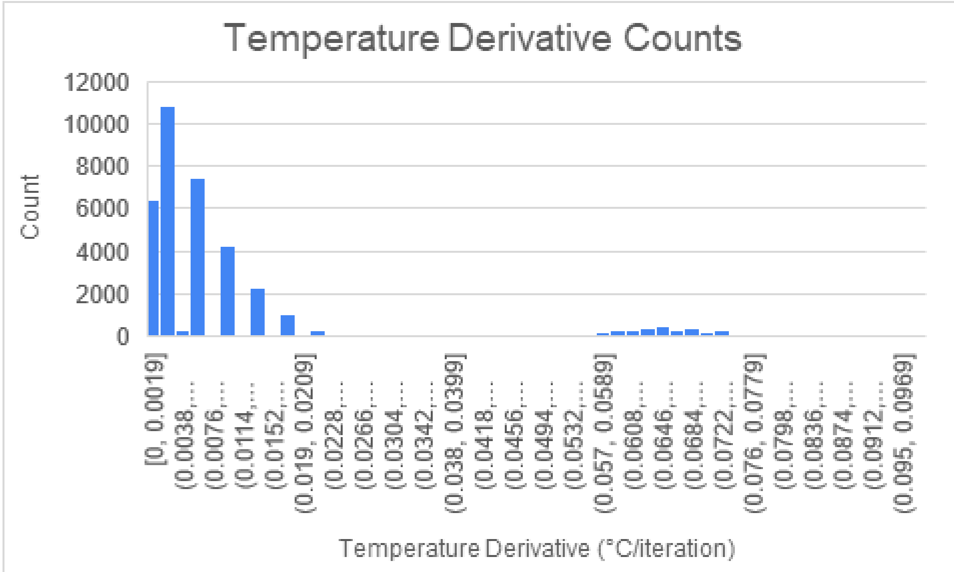

Figure 5.1: A histogram of changes in temperature for a standard run of the liquid nitrogen cooling system with electromagnetic interference (EMI) causing noise.

An unfortunate consequence of the automatic refills of liquid nitrogen (”autofills”) from the industrial source to the dewar that contains our resistors is that during these periods of time the increase in pressure pushes additional nitrogen vapor into our thermos, resulting in unintended cooling. The LabVIEW program automatically reacts to the temperature being colder than the set temperature and does not run the resistors during this time, which has an unintended result. Once the automatic refill to the small dewar is complete, the temperature begins to drift up from a new minimum well below the set temperature, as seen in Figure 5.2. This results in a sustained period where the resistors do not burn liquid nitrogen. During this time, the transfer line begins to heat up rapidly towards room temperature and if not interfered with, the temperature in the thermos will drift up substantially while the cooling system takes time to cool the transfer line again. It is proposed that this issue was partially responsible for the inadequate temperature control in the January 2023 Irradiation. In order to counter this problem, the program identifies when the thermos is more than 2 degrees below the set temperature and identifies this as a result of an autofill. Once the temperature begins to drift up after the autofill, the program tracks the rate of change of temperature and burns additional liquid nitrogen to limit it.

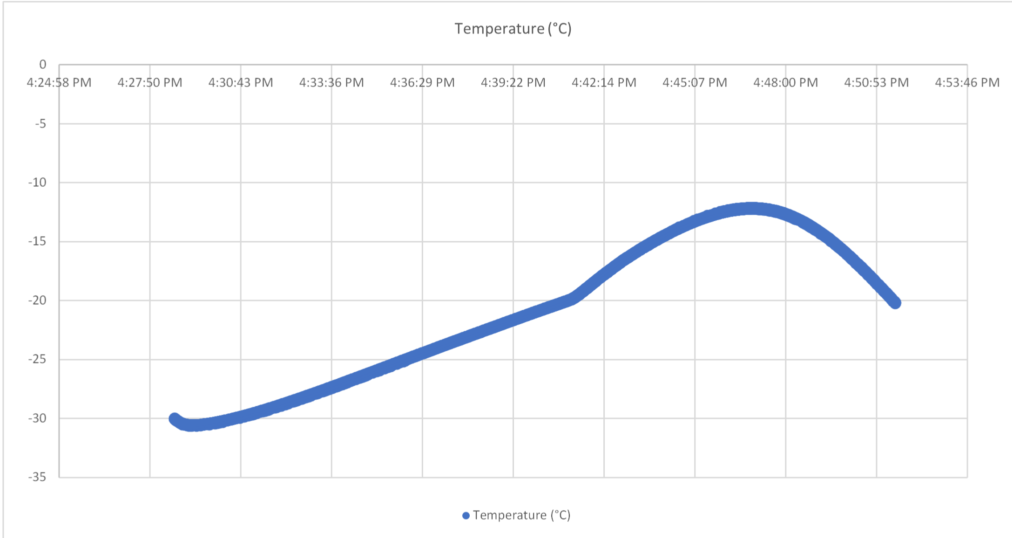

Figure 5.2: Temperature data after an autofill without the problem addressed. The set temperature for the LabVIEW program was -20 °C so the resistors were turned off until the set temperature was reached, causing a time delay where the nitrogen vapor cooled the transfer line before cooling the thermos again. During this time the temperature in the thermos rose 8 degrees over the set temperature.

As seen in Figures 5.3 and 5.4, cooling tests maintain temperatures within +/- 0.5 °C with the updated cooling system except during autofill periods. After autofills, the temperature did not exceed the set temperature of -20 °C by an unreasonable amount, returning to the standard equilibrium state. Both plots use data with long thermocouple lines, so EMI is expected. With successful temperature control now established, the results of a future irradiation should be more reliable.

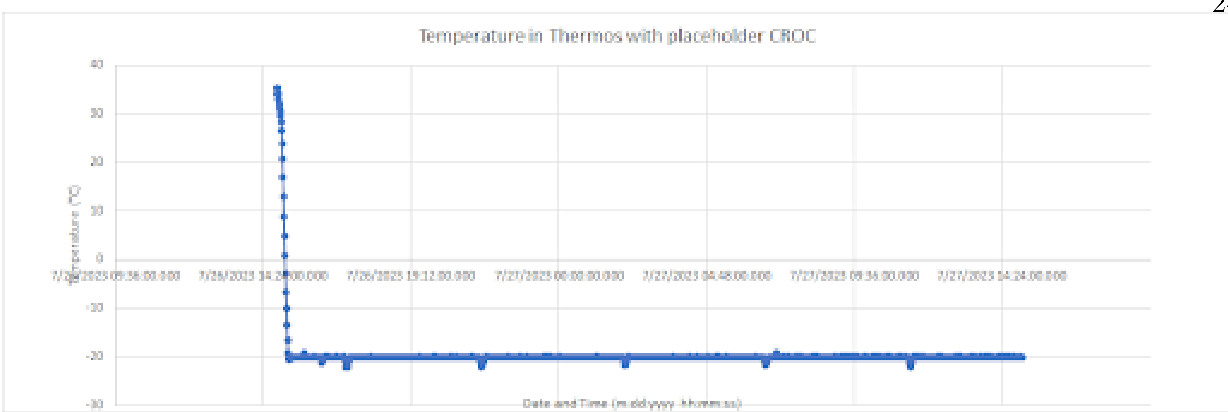

Figure 5.3: Plot of a successful cooling test with several autofills. Cooled from room temperature with a ROC providing a heat load and a set temperature of -20 °C. Resistors ran after autofill completed to prevent overheating.

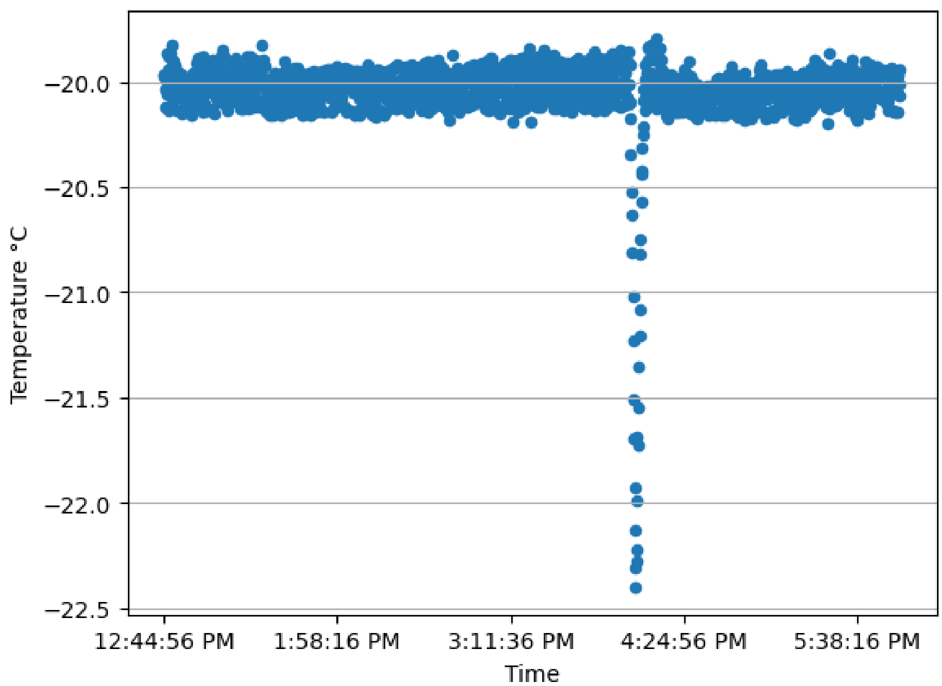

Figure 5.4: Plot of a cooling test focused on response to a single autofill with the problem addressed. There is a longer timescale after the autofill is complete due to the resistors running. Time spent above the set temperature after the autofill is comparable to standard operation, a strong result when compared with Figure 5.2.

Chapter 6

Future Work

Now that proper temperature control has been established, future irradiation tests have the potential to give stronger results. A follow up irradiation at the Gamma Irradiation Facility is likely in the near future. A possible direction of further tests could include irradiation tests at various other temperatures. Other tests on silicon detectors have been performed at -30 °C. With the liquid nitrogen cooling system able to maintain temperatures below -20 °C consistently, the main trade off is increased liquid nitrogen use. Due to its effectiveness in high radiation environments, the liquid nitrogen cooling system may have applicability in other small-scale particle physics instrumentation experiments. This may allow the pursuit of other methods of irradiation at other national laboratories, with different sources of radiation than Cobalt-60 gammas. Despite the total integrated dose desired during our tests being representative of the lifetime dose planned for CMS, a more representative dose rate over a longer timescale could have interesting results.

Chapter 7

Conclusion

The HL-LHC and CMS Experiment Phase-2 upgrades show great promise in continuing the search for physics beyond the Standard Model. The exciting improvements will increase resolution, but they will incur great challenges on the experiment's components, specifically on those in the inner tracker of CMS. The success of the inner tracker will rely on the radiation hardness of the silicon pixel sensors and their attached readout chips. While a previous attempt to to assess radiation hardness via ^{60}Co gamma irradiation failed, improvements have been made that should allow a conclusive result in the near future. Development of the liquid nitrogen cooling system is complete, with plans to return to Sandia National Laboratories in November 2023. With adequate liquid nitrogen provided, this cooling system can run unattended for over 60 hours.

Bibliography

[1] CERN "High-Luminosity LHC" Accessed: Nov. 01, 2023. [Online]. Available: https://home.cern/science/accelerators/high-luminosity-lhc

[2] "New paradigms for the CMS Phase-2 Upgrades — CMS Experiment." Accessed: Nov. 01, 2023. [Online]. Available: https://cms.cern/news/new-paradigms-cms-phase-2-upgrades

[3] B. Pierre et al. 'RD53 chip progress', Aix-Marseille University, France, 2021. URL: https://indico.in2p3.fr/event/20437/contributions/99775/attachments/66357/92747/20211013JMEMenouni.pdf

[4] M. P. Rauch "Thermal Measurements and Characterizations for the CMS Phase-1 Barrel Pixel Detector and the CMS Phase-2 Upgrade Tracker 2S Module with Evaporative CO2 Cooling Systems," Ph.D. dissertation, RWTH Aachen U., 2020, https://cds.cern.ch/record/2740861/export/hx?ln=en

[5] "Silicon Strips — CMS Experiment." Accessed: Oct. 28, 2023. [Online]. Available: https://cms.cern/detector/identifying-tracks/silicon-strips

[6] T. Heim 'Test Results from the RD53A Pixel readout chip and Design Status of its Successor', Hiroshima, 2019. URL: https://indico.cern.ch/event/803258/contributions/3582903/attachments/1962498/3263619/316HEIMrd53.pdf

[7] S. J. Pearton et al., "Review—Radiation Damage in Wide and Ultra-Wide Bandgap Semiconductors," ECS J. Solid State Sci. Technol., vol. 10, no. 5, p. 055008, May 2021, doi: 10.1149/2162-8777/abfc23.

[8] "Particle Data Group," Particle Data Group. Accessed: Nov. 01, 2023. [Online]. Available: https://pdg.lbl.gov/

[9] "CMS Detector Design — CMS Experiment." Accessed: Nov. 01, 2023. [Online]. Available: https://cms.cern/news/cms-detector-design

[10] G. L. Bayatian et al., "CMS Physics Technical Design Report: Addendum on High Density QCD with Heavy Ions," Jan. 2007.

[11] "Silicon Pixels — CMS Experiment." Accessed: Nov. 01, 2023. [Online]. Available: https://cms.cern/detector/identifying-tracks/silicon-pixels/

[12] W. Adam et al., "P-Type Silicon Strip Sensors for the new CMS Tracker at HL-LHC," J. Inst., vol. 12, no. 06, p. P06018, Jun. 2017, doi: 10.1088/1748-0221/12/06/P06018.

[13] "Beta Decay Examples." Accessed: Nov. 01, 2023. [Online]. Available: http://hyperphysics.phy-astr.gsu.edu/hbase/Nuclear/betaex.html

[14] J. H. Hubbell, H. A. Gimm, and I. Øverbø, "Pair, Triplet, and Total Atomic Cross Sections (and Mass Attenuation Coefficients) for 1 MeV-100 GeV Photons in Elements Z =1 to 100," Journal of Physical and Chemical Reference Data, vol. 9, no. 4, pp. 1023–1148, Oct. 1980, doi: 10.1063/1.555629.

[15] P. Pattison, "X-ray and gamma-ray Compton scattering," phd, University of Warwick, 1975. Accessed: Nov. 01, 2023. [Online]. Available: http://webcat.warwick.ac.uk/record=b1747608~S15

[16] S. Biereigel, S. Kulis, P. Leroux, P. Moreira, and J. Prinzie, "Radiation-Tolerant Digitally Controlled Ring Oscillator in 65-nm CMOS," IEEE Trans. Nucl. Sci., vol. 69, no. 1, pp. 17–25, Jan. 2022, doi: 10.1109/TNS.2021.3132402.

[17] C. Kierans, T. Takahashi, and G. Kanbach, Compton Telescopes for Gamma-ray Astrophysics. 2022.

[18] Inductiveload, English: A ring oscillator constructed from three inverters in series. 2009. Accessed: Nov. 01, 2023. [Online]. Available: https://commons.wikimedia.org/wiki/File:Ring_oscillator_(3-stage).svg

[19] J. Cumalat et al., "Irradiation of CROC 201.57 with 60Co γ s at Sandia National Lab," in preparation.

[20] REOTEMP Instruments "Type K Thermocouple" Accessed: Nov. 01, 2023. [Online]. Available: https://www.thermocoupleinfo.com/type-k-thermocouple.htm